

Improving the Oxygen Evolution Reaction: Exsolved Cobalt Nanoparticles on Titanate Perovskite Catalyst

Shangshang Zuo, Yuan Liao, Chenchen Wang, Aaron B. Naden, and John T. S. Irvine*

Perovskites are an important class of oxygen evolution reaction (OER) catalysts due to highly tunable compositions and adaptable characteristics. However, perovskite-based catalysts can have limited atom utilization efficiency due to large particle size, resulting in low mass activity. Herein, Cobalt nanoparticles are exsolved from $\text{La}_{0.2+2x}\text{Ca}_{0.7-2x}\text{Ti}_{1-x}\text{Co}_x\text{O}_3$ perovskite and applied in OER. Upon reduction in the 5% H_2/N_2 atmosphere at 800 °C for 2 h, the Co exsolved perovskite catalyst (R-LCTCo0.11) exhibits optimal OER performance. The mass activity of R-LCTCo0.11 reaches $\approx 1700 \text{ mA mg}^{-1}$ at an overpotential of 450 mV, which is 17 times and 3 times higher than that of LCTCo0.11 (97 mA mg^{-1}) and R-Mix (560 mA mg^{-1}) catalysts respectively, surpassing the benchmark catalyst RuO_2 (42.7 mA mg^{-1} of oxide at $\eta = 470 \text{ mV}$). Electrochemical impedance spectroscopy (EIS) data reveals that R-LCTCo0.11 has the lowest charge transfer resistance ($R_{\text{ct}} = 58 \Omega$), demonstrating the highest catalytic and kinetic activity for OER. Furthermore, this catalyst shows high stability during an accelerated durability test of 10 h electrolysis and 1000 cycles cyclic voltammetry (CV). This work demonstrates that nanoparticle exsolution from a doped perovskite is an effective strategy for improving the atom utilization efficiency in OER.

for OER is pivotal to promote reaction dynamics in practical hydrogen production.^[3,4] So far, precious metal-based electrocatalysts, such as RuO_2 and IrO_2 , exhibit excellent OER performance in both acidic and alkaline electrolytes, but their high cost and scarcity on earth constrain large-scale applications.^[4–6] Thus, the design and synthesis of non-precious metal-based OER electrocatalysts with low cost and earth abundance has attracted extensive interest in recent years.^[7–9]

Recently, perovskite oxides (i.e., ABO_3 , where A in this structure is typically occupied by an alkali/alkaline earth/rare earth element with a 12-fold coordination and B is generally held by a transition metal element with a 6-fold coordination with oxygen)^[10] have spurred multiple waves of interest for OER catalysis due to their highly tunable compositions and adaptable physicochemical characteristics.^[7,11–13] For instance, the $\text{Ba}_{0.5}\text{Sr}_{0.5}\text{Co}_{0.8}\text{Fe}_{0.2}\text{O}_{3-\delta}$ (BSCF) catalyst displays excellent OER performance, even higher than that of IrO_2 for the intrinsic


activity.^[11] Lee et al. make use of in situ conversion of BaNiO_3 during OER to obtain a new family of perovskite $\text{BaNi}_{0.83}\text{O}_{2.5}$ with ideal O 2p band structure, which surpasses many perovskite oxides in OER activity.^[14] However, the large particle size of perovskite-based catalysts could limit their atom utilization efficiency, leading to low mass activity. Many approaches have been developed to improve the mass activity, such as ball-milling method, plasma process, tailoring the surface cation configuration, and construct microstructures on the catalyst surface.^[15–19] However, the nanoparticle agglomeration is very likely to occur during synthesis or ageing process because of the property of unanchored nanoparticles. As a matter of fact, anchored nanoparticles could be exsolved from the perovskite framework, which has been recently extensively exploited in high-temperature fuel cells.^[20–28] It is reported that exsolution is tunable by varying vacancies, compositions, calcination temperature, and atmosphere.^[29] As an illustration, the presence of A-site vacancies can serve as a compelling driving force facilitating the exsolution of B-site elements to reinstate stoichiometry.^[29] Through this process, certain metal nanoparticles could be anchored on the perovskite surface, which could avoid nanoparticle agglomeration to achieve higher mass activity.

To the best of our knowledge, the exsolution of metal nanoparticles from perovskites is rarely investigated as

1. Introduction

Water electrolysis, as an ideal method of utilizing renewable energy sources such as solar, tidal, and wind energy, has gained increasing attention in light of the current energy shortage and climate emergency situation.^[1] Water electrolysis involves the hydrogen evolution reaction (HER) at the cathode and oxygen evolution reaction (OER) at the anode. Although water electrolysis is considered one of the most efficient and reliable technologies for large-scale hydrogen production,^[2] it is still hampered by the sluggish four-electron transfer kinetics in OER. Therefore, developing potential electrocatalysts

S. Zuo, Y. Liao, C. Wang, A. B. Naden, J. T. S. Irvine
School of Chemistry
University of St Andrews
St Andrews, Fife KY16 9ST, UK
E-mail: jtsi@st-andrews.ac.uk

 The ORCID identification number(s) for the author(s) of this article can be found under <https://doi.org/10.1002/small.202308867>

© 2023 The Authors. Small published by Wiley-VCH GmbH. This is an open access article under the terms of the Creative Commons Attribution License, which permits use, distribution and reproduction in any medium, provided the original work is properly cited.

DOI: 10.1002/small.202308867

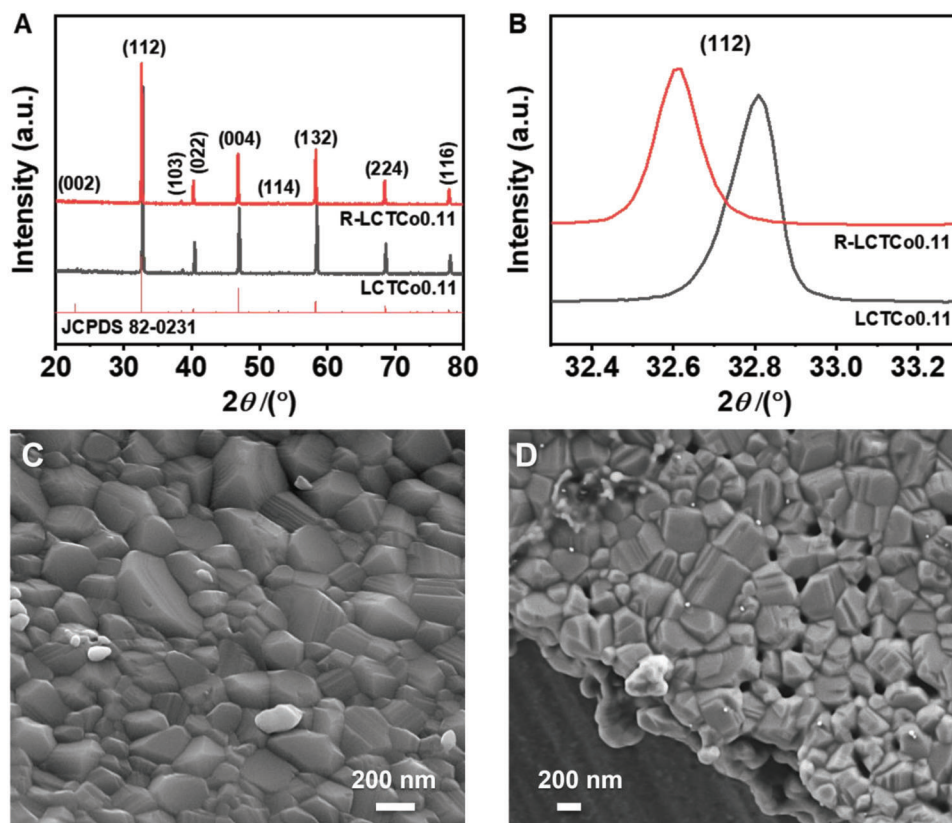


Figure 1. A) Room temperature X-ray diffraction patterns of LCTCo0.11 and R-LCTCo0.11, and B) corresponding magnified XRD patterns of peak (112). SEM images of C) LCTCo0.11, and D) R-LCTCo0.11.

low-temperature OER catalysts. In this work, a series of Co-doped $\text{La}_{0.2+2x}\text{Ca}_{0.7-2x}\text{Ti}_{1-x}\text{Co}_x\text{O}_3$ (LCTCo $_x$, $x = 0.01, 0.05, 0.11, 0.2,$ and 0.3) perovskites are synthesized, and Co nanoparticles are successfully exsolved from the parent perovskite after calcination in a reducing atmosphere. To optimize catalyst performance, Co doping level, reduction temperature, and time have been explored. The optimized catalyst (R-LCTCo0.11, reduced from LCTCo0.11 at 800 °C for 2 h in a 5% H_2/N_2 atmosphere) exhibits 17-times of mass activity compared with the parent perovskite (LCTCo0.11) at an overpotential of 450 mV. The relevant mechanism is also explained by electrochemical impedance spectroscopy (EIS) results. This work shows the great potential of metal exsolution from the perovskite framework to improve the atom utilization efficiency and promising development toward OER.

2. Results and Discussion

2.1. Structure Characterization

The phase components and crystal structures of as-synthesized LCTCo0.11 and R-LCTCo0.11 are represented through X-ray Diffraction (XRD) patterns. As shown in **Figure 1A**, the diffraction peaks of LCTCo0.11 and R-LCTCo0.11 observed at 22.9, 32.6, 38.5, 40.2, 46.8, 52.8, 58.3, 68.5, and 77.9° are well indexed with (002), (112), (103), (022), (004), (114), (132), (224), and (116) crystal planes of CaTiO_3 (JCPDS 82–0231), which belong to the phase

of orthorhombic structure (space group Pbnm, no. 62). It is obvious the introduction of Co does not change the structure of CaTiO_3 . Additionally, energy dispersive spectroscopy (EDS) of the samples LCTCo0.11 and R-LCTCo0.11 confirmed the presence of the elements La, Ca, Ti, Co, and O, respectively (Figure S1, Supporting Information). These results indicate successful synthesis of Co-doped lanthanum calcium titanate perovskite. According to magnified XRD patterns in **Figure 1B**, the perovskite (112) reflection shifts to lower 2θ angles after reduction, indicating larger cell parameters, which is consistent with the refinement data (**Table 1**). As seen in **Table 1**, the lattice parameters of LCTCo0.11 are $a = 5.471 \text{ \AA}$, $b = 5.472 \text{ \AA}$, and $c = 7.738 \text{ \AA}$, which are all smaller than that of R-LCTCo0.11 ($a = 5.473 \text{ \AA}$, $b = 5.475 \text{ \AA}$, and $c = 7.744 \text{ \AA}$). This can be explained by the transformation of smaller Ti^{4+} (0.605 Å) to larger Ti^{3+} (0.67 Å) on the B-site as well as associated oxygen loss.^[30] It can be seen clearly in SEM images of **Figure 1C,D** that the cobalt nanoparticles have been generated on the surface of LCTCo0.11 after 2 h reduction at 800 °C and the diameter of the particles is $\approx 30 \text{ nm}$.

Additionally, based on the XRD patterns shown in **Figure S2** (Supporting Information), the reference sample LCT ($\text{La}_{0.2}\text{Ca}_{0.7}\text{TiO}_3$) exhibits a pure phase that corresponds well with JCPDS 82–0231, while the CoOy sample (synthesized using the same sol–gel method as the other samples) exhibits a predominant Co_3O_4 phase with a minor CoO phase. The Mix sample is obtained by combining the LCT and CoOy components, resulting in the presence of two phases, CaTiO_3 and

Table 1. Refined unit-cell lattice parameters of LCTCo0.11 and R-LCTCo0.11.

Sample	Symmetry	Space group	Refined Cell parameters [Å]			Cell volume [Å ³]
			a	B	c	
LCTCo0.11	Orthorhombic P	Pbnm (62)	5.471	5.472	7.738	231.65
R-LCTCo0.11	Orthorhombic P	Pbnm (62)	5.473	5.475	7.744	232.05

Co₃O₄, as indicated by the XRD pattern. However, upon reduction, the Co₃O₄ phase becomes indiscernible, while the presence of cobalt phase is observable in the R-Mix sample (reduced from Mix sample at 800 °C for 2 h in a 5% H₂/N₂ atmosphere), as indicated by the XRD pattern (Figure S2, Supporting Information). Correspondingly, SEM images in Figure S3 (Supporting Information) reveal consistent findings. Notably, the identification of the sub-micrometer spherical structure in the SEM image (Figure S3D, (Supporting Information)) becomes challenging due to its degradation after reduction, ultimately leading to the absence of the Co₃O₄ phase in the XRD pattern of the R-Mix sample (Figure S2, (Supporting Information)).

Furthermore, a series of LCTCox and R-LCTCox₁₀ h (reduced from LCTCox at 800 °C for 10 h in a 5% H₂/N₂ atmosphere) samples with various Co doping levels have been prepared and investigated. As displayed in Figure S4 (Supporting Information) the crystal structure of LCTCox is indexed with CaTiO₃ (JCPDS 81–0561) and the (112) peak shifts to lower 2θ angles with the increase of Co doping level, indicating higher interplanar spacing, which agrees with the refined unit cell parameters (Figure S9; Table S1, Supporting Information). Figure S5A (Supporting Information) illustrates that most of the peaks of R-LCTCox₁₀ h samples can be well indexed to CaTiO₃ (JCPDS 82–0230) except for the small peak at 44.2° (belonging to cobalt (JCPDS 15–0806)) that can only be observed in samples R-LCTCo0.2₁₀ h and R-LCTCo0.3₁₀ h due to the higher exsolved amount. The analysis of Figure S5B to F (Supporting Information) clearly reveals a correlation between the Co doping level and the size and quantity of exsolved Co nanoparticles. When the Co doping level is 0.01, it becomes challenging to detect Co nanoparticles (as depicted in Figure S5B, Supporting Information). However, as the Co doping level increases to 0.05, the Co nanoparticles exhibit a diameter of ≈70 nm (as illustrated in Figure S5C, Supporting Information). The exsolved Co nanoparticles obtained from R-LCTCo0.11₁₀ h (Figure S5D, Supporting Information) display a size range of 80–110 nm. Notably, Figure S5E (Supporting Information) demonstrates the onset of agglomeration as the Co doping level reaches 0.2. Furthermore, Figure S5F (Supporting Information) provides evidence that Co nanoparticles can attain sizes up to 210 nm.

Moreover, LCTCo0.11 has been calcined at 800 °C in a tubular furnace in a 5% H₂/N₂ atmosphere for various calcination times. The diffraction peaks of these samples in Figure S6A (Supporting Information) correspond to CaTiO₃ (JCPDS 82–0231), which belongs to the phase of orthorhombic structure with the space group of Pbnm (62). As shown from Figure S6B to F (Supporting Information), it is quite apparent that the size of exsolved Co nanoparticles grows with the extent of reduction time. The diameter of the exsolved Co nanoparticles in the R-LCTCo0.11_{0.5} h sample (Figure S6B, Supporting Information) is ≈10 nm and in-

creases to 30 nm when the calcining time is extended by ten times (R-LCTCo0.11₅ h, Figure S6E, Supporting Information). Finally, after 10 h of calcination, the size of the Co nanoparticles could reach 100 nm (R-LCTCo0.11₁₀ h, Figure S6F, Supporting Information). Besides, the effects of calcination temperature on the R-LCTCo0.11₂ h catalysts (reduced from LCTCo0.11 at various temperatures for 2 h in a 5% H₂/N₂ atmosphere) have been investigated. XRD patterns of the as-prepared R-LCTCo0.11₂ h samples are shown in Figure S7 (Supporting Information). All these samples exhibit a pure orthorhombic structure with the space group Pbnm (no. 62). The SEM images presented in Figure S8 (Supporting Information) indicate that the Co nanoparticles on R-LCTCo0.11₆₀₀ °C and R-LCTCo0.11₇₀₀ °C exhibit a similar size of ≈30 nm. The particle size of exsolved Co slightly increases by increasing the reduction temperature, but it remains less than 50 nm even at a high temperature of 900 °C for 2 h (Figure S8D, Supporting Information). In conclusion, the reduction temperature shows a relatively slight impact on the particle size of the exsolved Co compared to other conditions.

To study the effect of different synthesis conditions on the crystal structure, cell parameter refinement of all the perovskite samples mentioned above are carried out and summarized in Figure S9 and Tables S1 to S4 (Supporting Information). As exhibited in Figure S9A,B (Supporting Information), with an increase of Co doping level, their unit-cell parameters and volume expand. In contrast, reduction time and temperature have an inconspicuous influence on the unit-cell parameters (Figure S9C,D, Supporting Information).

Scanning Transmission Electron Microscopy (STEM) technology is introduced to get a better understanding of the atomic structures of LCTCo0.11 and R-LCTCo0.11. The STEM image and the corresponding elemental mapping images in Figure S10 (Supporting Information) suggest that the component elements of LCTCo0.11 are distributed uniformly, which proves that the doped Co is spread evenly in the bulk material instead of being split into enormous aggregates. The atomic-resolution high-angle annular dark-field (HAADF) STEM images recorded along the [110] zone axis of LCTCo0.11 is displayed in **Figure 2A**. The interplanar spacing of (112) of LCTCo0.11 is measured to be 0.273 nm, as a comparison, the (112) lattice plane spacing of R-LCTCo0.11 is increased to 0.292 nm (the inset in Figure 2B), which is well-consistent with the XRD data in Figure 1B. Figure 2A also depicts the schematic diagram of atomic configuration of LCTCo0.11 along the [110] direction, as well as the orthorhombic perovskite unit cell. The STEM and corresponding EDS elemental distribution mapping images in Figure 2B reveal that the Co nanoparticles have been successfully exsolved from the bulk perovskite and that the diameter of the Co nanoparticle is ≈30 nm, which is in line with the SEM data (Figure 1D).

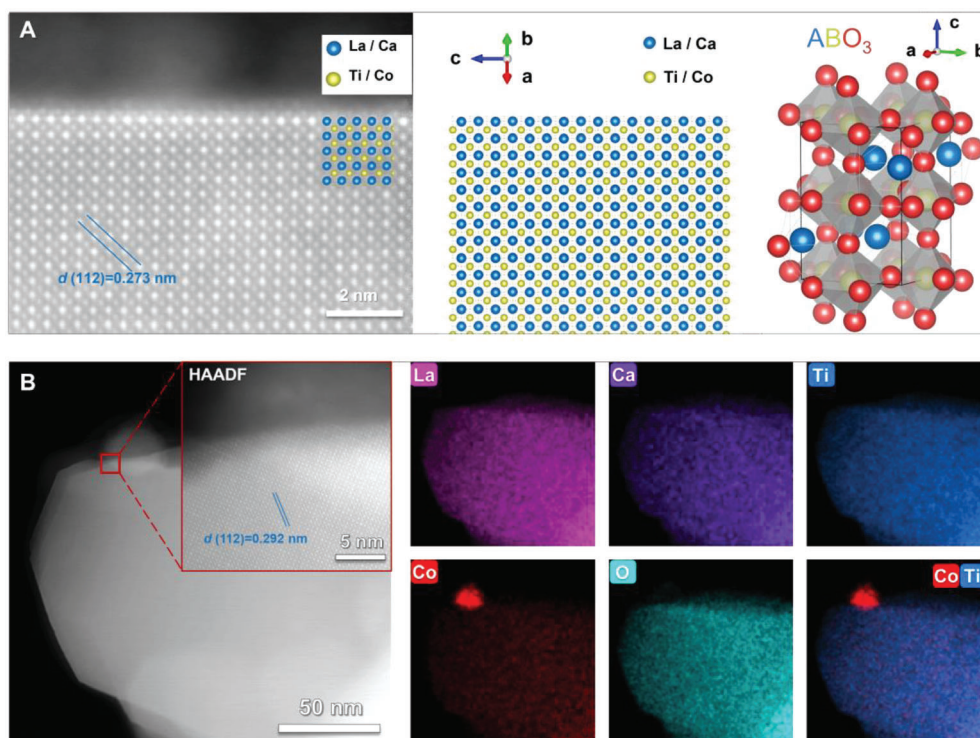


Figure 2. A) HAADF-STEM image with corresponding schematic along the [110] zone axis and the crystal structure of orthorhombic perovskite for LCTCo0.11. B) HAADF-STEM images with corresponding EDS elemental distribution mapping of R-LCTCo0.11.

The adsorption and desorption isotherms of N_2 at 77 K and the corresponding physical properties (pore size distribution, BET specific surface area and pore volume) for the prepared samples are shown in Figure S11 (Supporting Information). According to the IUPAC classification, the adsorption isotherms for all samples are Type IV implying the mesoporous structures.^[31] All of the isotherms rise sharply, approaching $P/P_0 = 1$, indicating the presence of macropores (pore size > 50 nm), which agrees well with the pore size distribution curves in Figure S11B (Supporting Information).^[31] The pore size distribution of all samples centers ≈ 120 and 140 nm. Figure S11C (Supporting Information) demonstrates that Mix and R-Mix samples have the largest special surface area (SSA), $\approx 5 \text{ m}^2 \text{ g}^{-1}$, while the SSA of LCT is $4.1 \text{ m}^2 \text{ g}^{-1}$, which is higher than that of LCTCo0.11 ($0.9 \text{ m}^2 \text{ g}^{-1}$) and R-LCTCo0.11 ($2.5 \text{ m}^2 \text{ g}^{-1}$). The pore volumes of LCTCo0.11 ($0.002 \text{ cm}^3 \text{ g}^{-1}$) and R-LCTCo0.11 ($0.006 \text{ cm}^3 \text{ g}^{-1}$) in Figure S11D (Supporting Information) rank last and second to last, respectively. However, this time, LCT ($0.021 \text{ cm}^3 \text{ g}^{-1}$) has the highest pore volume, and the Mix sample exhibits a similar pore volume of $0.011 \text{ cm}^3 \text{ g}^{-1}$ to that of R-Mix. To reveal the amount of exsolved Co nanoparticles, thermogravimetric analysis (TGA) result of R-LCTCo0.11 is depicted in Figure S12 (Supporting Information). The R-LCTCo0.11 experienced an overall weight gain of $\approx 1.00\%$ once the temperature reached $530 \text{ }^\circ\text{C}$. This increase in weight can be mainly attributed to the re-oxidation of the Co nanoparticles, which resulted in the formation of Co_3O_4 nanoparticles.^[32] Consequently, the mass ratio of exsolved Co nanoparticles did not exceed 2.75%.

2.2. OER Performance

To investigate the potential of exsolution from perovskite on low-temperature electrocatalysis, the OER performance of R-LCTCo0.11 and corresponding control samples is evaluated in 1.0 M KOH. First of all, the OER activities on LCT, Mix, R-Mix, LCTCo0.11, and R-LCTCo0.11 are measured by Linear sweep voltammetry (LSV) and all the measured LSV curves in this study are iR -corrected. As shown in Figure 3A, LCT, Mix, and LCTCo0.11 exhibit negligible performance toward OER. Regarding the overpotential (η) to support a current density of 10 mA cm^{-2} , R-LCTCo0.11 delivers an overpotential of 430 mV, which is lower than R-Mix ($\eta = 481 \text{ mV}$) sample and even comparable to the benchmark catalysts of BSCF (420 mV) and IrO_2 (440 mV).^[33]

To acquire a deep understanding of catalytic kinetics, the Tafel plots obtained from polarization curves are displayed in Figure 3B. The Tafel slopes of LCT, Mix, and LCTCo0.11 are 118, 120, and 117 mV dec^{-1} , respectively, suggesting that the first stage is the rate-determining step (corresponding featured Tafel slope: 120 mV dec^{-1}) for LCT, Mix, and LCTCo0.11 in the OER process, where the -OH groups are strongly bonded with the catalyst, making the deprotonation process hard to occur.^[34] As a comparison, the Tafel slopes for R-Mix and R-LCTCo0.11 significantly drops to 62.7 and 53.5 mV dec^{-1} , respectively, indicating a different rate-determining step because of the closeness to another featured Tafel slope of 60 mV dec^{-1} .^[34] Besides, R-LCTCo0.11 displays the smallest Tafel slope, implying the fastest OER rate among these tested catalysts.

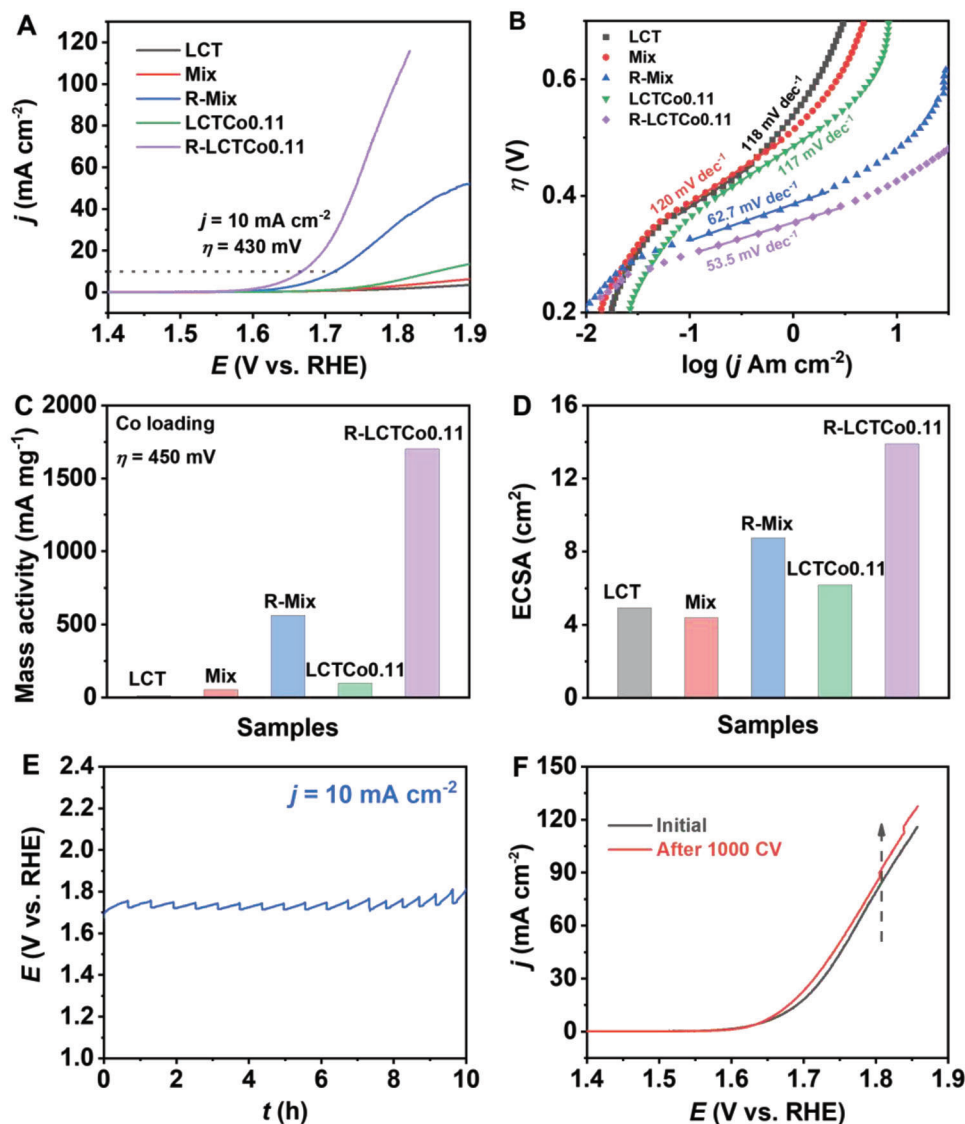


Figure 3. A) LSV curves, B) Tafel plots of LCT, Mix, R-Mix, LCTCo0.11, and R-LCTCo0.11 catalysts recorded in 1.0 M KOH. C) Mass activities based on the amount of Co loading at $\eta = 450$ mV, and D) ECSA of LCT, Mix, R-Mix, LCTCo0.11, and R-LCTCo0.11 catalysts. E) Chronopotentiometry test for R-LCTCo0.11 at a current density of 10 mA cm^{-2} without iR -correction. F) LSV curves of R-LCTCo0.11 obtained initial and after 1000 cycles of accelerated CV.

Motivating high catalytic performance while maintaining low metal loading has been a critical issue in catalyst design since it is directly related to catalyst cost and commercial application.^[35] Figure 3C plots the mass activities (based on the amount of Co loading) of LCT, Mix, R-Mix, LCTCo0.11, and R-LCTCo0.11 catalysts at an overpotential of 450 mV. Notably, the mass activity of R-LCTCo0.11 reaches $\approx 1700 \text{ mA mg}^{-1}$, which is 3-times and 17-times higher than R-Mix (560 mA mg^{-1}) and LCTCo0.11 (97 mA mg^{-1}), respectively. And definitely surpasses the benchmark catalyst RuO_2 (42.7 mA mg^{-1} of oxide at $\eta = 470$ mV),^[36] suggesting the excellent OER catalytic performance of the Co nanoparticles anchored perovskite catalyst. The OER mass activity of R-LCTCo0.11 is remarkable compared to the most reported state-of-the-art OER electrocatalysts (Table S5, Supporting Information), making it has potential for practical applications. The

mass activities for the rest of the samples are insignificant compared with R-LCTCo0.11. Meanwhile, the electrochemically active surface area (ECSA) of LCT, Mix, R-Mix, LCTCo0.11, and R-LCTCo0.11 have also been compared (Figure 3D), which are derived from Figures S13–S15 (Supporting Information). The as-prepared LCT shows an ECSA of 4.92 cm^2 , then increased to 6.155 cm^2 after doping of 11% cobalt (LCTCo0.11), and it finally reaches to 13.888 cm^2 after the exsolution of cobalt nanoparticles (R-LCTCo0.11). The ECSA of Mix is 4.383 cm^2 , which is lower than LCTCo0.11, and rises up to 8.738 cm^2 after reduction. This is similar to the ECSA trend from LCTCo0.11 to R-LCTCo0.11. The results unequivocally demonstrate that the increase in Co utilization from exsolution of perovskite can improve the OER performance. The stability of R-LCTCo0.11 is measured by chronopotentiometry at $j = 10 \text{ mA cm}^{-2}$ and 1000 cycles cyclic voltammetry

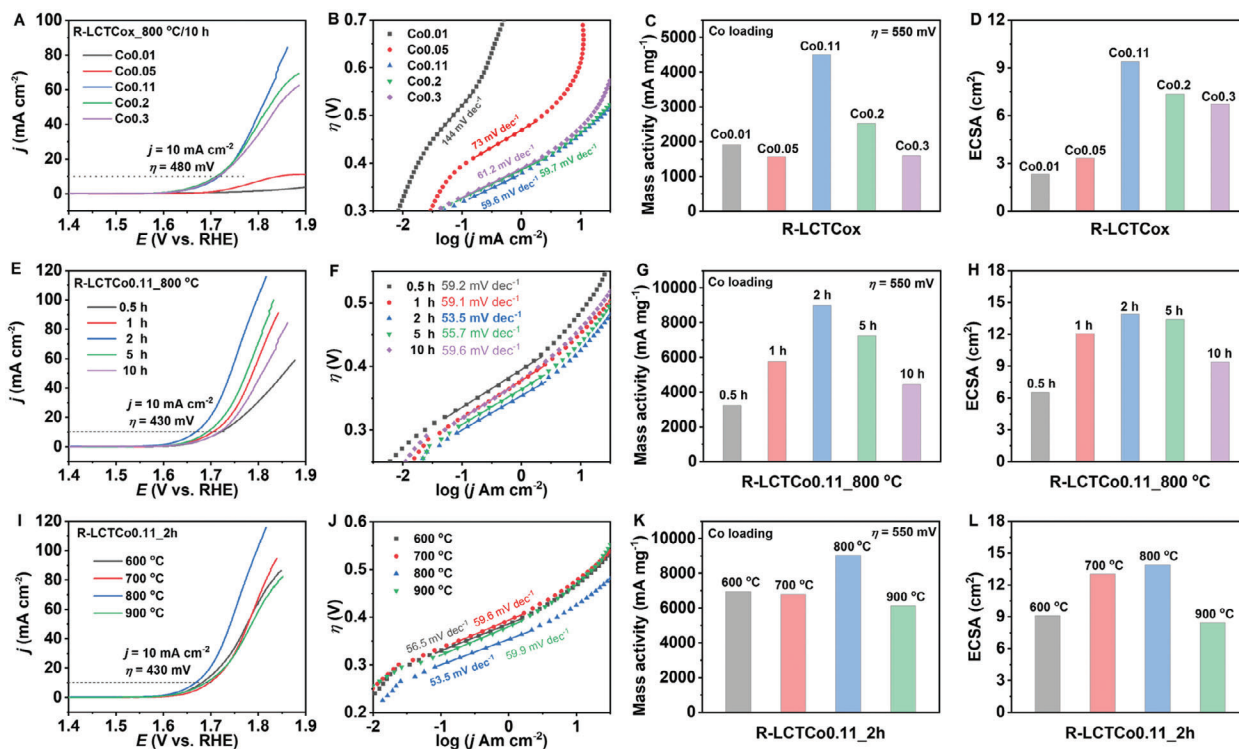


Figure 4. A) LSV curves, B) Tafel plots, C) mass activities based on the amount of Co loading at $\eta = 550$ mV, and D) ECSA (derived from Figures S16–S18, Supporting Information) of R-LTCo_x_10 h ($x = 0.01, 0.05, 0.11, 0.2,$ and 0.3), which were prepared in a tubular furnace at 800 °C for 10 h in 5% H_2/N_2 atmosphere. E) LSV curves, F) Tafel plots, G) mass activities based on the amount of Co loading at $\eta = 550$ mV, and H) ECSA (derived from Figures S19–S21, Supporting Information) of R-LTCo_{0.11}_800 °C, which were produced in a tubular furnace at 800 °C for $0.5, 1, 2, 5,$ or 10 h in 5% H_2/N_2 atmosphere, respectively. I) LSV curves, J) Tafel plots, K) mass activities based on the amount of Co loading at $\eta = 550$ mV, and L) ECSA (derived from Figures S22 and S23, Supporting Information) of R-LTCo_{0.11}_2 h, which were produced in a tubular furnace at $600, 700, 800,$ or 900 °C for 2 h in 5% H_2/N_2 atmosphere, respectively.

(CV) as shown in Figure 3E,F. The results show that the catalyst of R-LTCo_{0.11} is remarkably durable under these aging conditions and its activity is even increased after 1000 cycles of CV scanning, which should be the result of in situ Co exsolution during the electrochemical process.^[35]

2.3. Optimization of OER Activities for R-LTCo_x

To optimize the performance of the R-LTCo_x catalyst, Co doping level, reduction time, and temperature have been explored. First, Figure 4A–D shows the OER activities of a series of R-LTCo_x_10 h electrocatalysts prepared at 800 °C for 10 h under a 5% H_2/N_2 atmosphere. The OER activities of R-LTCo_x increase sharply when the Co doping level is less than 11%, but then decreases slightly when the Co doping level reaches 20% and 30% (Figure 4A). The R-LTCo_{0.11}_10 h catalyst exhibits a Tafel slope of 59.6 mV dec⁻¹, lower than all the other samples, suggesting the fastest kinetics for OER (Figure 4B). Meanwhile, the R-LTCo_{0.11}_10 h catalyst delivers the highest mass activity and ECSA among all series of catalysts (Figure 4C,D). So, a doping level of 11% is selected for further studies.

Second, the relationship between reduction time and OER activity has been explored and the results are displayed in Figure 4E–H. LSV, mass activity, and ECSA all exhibit a similar

variation trend: they grow as the reduction time rises from 0.5 to 2 h, then decrease when the reduction time is extended to 5 and 10 h. However, all of the catalysts have comparable Tafel slopes, close to 60 mV dec⁻¹, indicating a similar mechanism for OER. In brief, the catalyst with 2 h reduction exhibits better OER performance. Additionally, the reduction temperature has also been studied, as indicated in Figure 4I–L. The LSV curves reveal that the R-LTCo_{0.11}_2 h catalyst synthesized at 800 °C displays the lowest overpotential of 430 mV at 10 mA cm⁻². The excellent OER activity is also revealed by the Tafel slope (53.5 mV dec⁻¹), mass activity (≈ 9000 mA mg⁻¹ of Co loading at $\eta = 550$ mV) and ECSA (13.888 cm²). In conclusion, it is clear that the R-LTCo_{0.11} catalyst reduced at 800 °C for 2 h shows the highest comprehensive performance toward OER in this research on account of the suitable amount and size of exsolved Co nanoparticles on the perovskite surface.

In order to investigate the relationship between structure and performance, we conducted a detailed analysis of the refined unit-cell lattice parameters for samples with different doping levels. The intriguing findings are presented in Figure 5. As shown in Table S1 (Supporting Information), while the structure of LTCo_{0.3} is cubic, the structures of all other samples are orthorhombic. By comparing the values of $a, b,$ and $c/\sqrt{2}$ in Figure 5A, we observe that the crystal structure of LTCo_{0.11} is the closest to the cubic structure among the

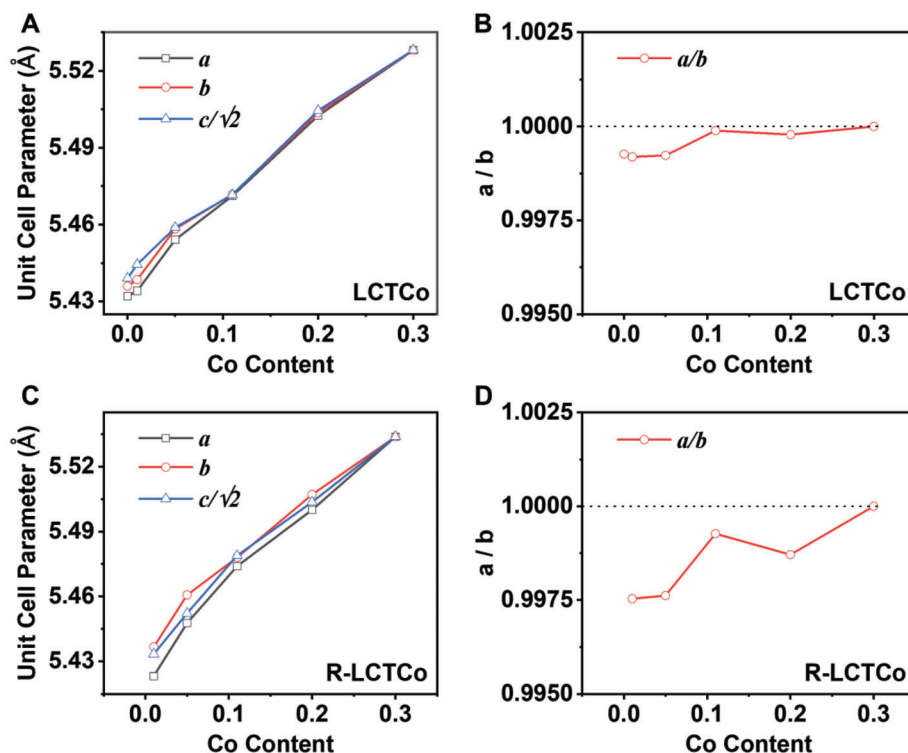


Figure 5. A) Refined unit-cell lattice parameters a , b , and $c/\sqrt{2}$ and B) a/b of LCTCo_x ($x = 0, 0.01, 0.05, 0.11, 0.2$, and 0.3). C) Refined unit-cell lattice parameters a , b , and $c/\sqrt{2}$ and D) a/b of R-LCTCo_x ($x = 0.01, 0.05, 0.11, 0.2$, and 0.3).

orthorhombic samples. Consequently, it is reasonable to find that the value of a/b in $\text{LCTCo}_{0.11}$ is the closest to 1 in Figure 5B. Remarkably, even in the corresponding reduced samples, they exhibit similar trends, as depicted in Figure 5C,D. Based on these compelling results, we can conclude that orthorhombic perovskite structures that approach cubic symmetry are more prone to the exsolution of Co nanoparticles with optimal size and density, which are highly advantageous for enhancing OER performance.

2.4. EIS Analysis

To further study the OER mechanisms of LCT, Mix, R-Mix, $\text{LCTCo}_{0.11}$, and $\text{R-LCTCo}_{0.11}$, EIS measurements were con-

ducted and are displayed in Figure 6 and Figure S24 (Supporting Information). According to Figure S24A,B (Supporting Information), the phase peak at lower frequency in LCT and Mix gradually shifts toward a higher frequency region with an increase in applied potential, indicating the characteristic frequency of active sites involved in OER. Meanwhile, the phase peak at a higher frequency remains stable and is not influenced by the applied external bias. This frequency range (10^2 – 10^3 Hz) corresponds to the surface double-layer capacitance (DLC).^[37] The corresponding Nyquist plots in Figure S24A',B' (Supporting Information) display two pseudo semicircles beyond onset potential. Hence, the equivalent electrical circuit (EEC) shown in Figure S25A (Supporting Information) is used to fit the EIS data of LCT and Mix obtained at 1.7 V versus RHE (Reversible Hydrogen Electrode).

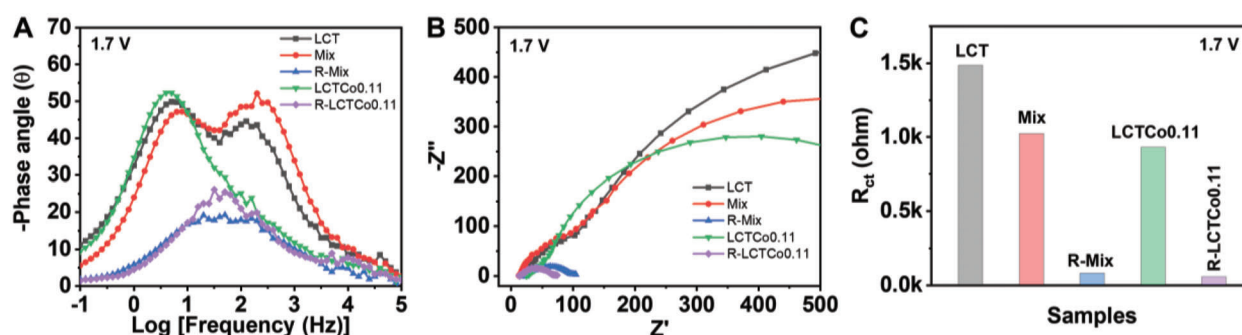


Figure 6. A) Bode impedance plots of LCT, Mix, R-Mix, $\text{LCTCo}_{0.11}$, and $\text{R-LCTCo}_{0.11}$ acquired at 1.7 V versus RHE. B) The corresponding Nyquist plots of the same samples. C) Plot of charge transfer resistance (R_{ct}) values for above samples at 1.7 V.

R_s represents the uncompensated electrolyte resistance, R_{ct1} is associated with the charge transfer rates within various steps in OER, and R_{ct2} is related to the adsorption resistance arising from reversibly adsorbed reactions.^[37,38] The total faradaic resistance for OER in this model is the sum of R_{ct1} and R_{ct2} , known as R_{ct} . The capacitor element is referred to as a constant phase element (CPE) due to its non-ideal impedance behavior.^[39] Figure S24C,D (Supporting Information) exhibits only one phase peak (R-Mix and LCTCo0.11), and the corresponding Nyquist plots (Figure S24C',D', Supporting Information) show a single semicircle. In this case, the Randle's cell model (Figure S25B, Supporting Information) can be used to analyze the EIS data. As for R-LCTCo0.11, the Bode plot shows two phase peaks in the potential range of 1.2–1.6 V, which then merge into a single peak when the potential exceeds 1.65 V, as shown in Figure S24E (Supporting Information). Similarly, the two pseudo semicircles in the Nyquist plot are transformed into a small pseudo semicircle in Figure S24E' (Supporting Information). Therefore, the Randle's model is also suitable for fitting the EIS data at 1.7 V. In the common Randle's model, R_s represents the uncompensated electrolyte resistance resulting from the interaction between the catalyst and electrolyte, while R_{ct} represents the charge transfer resistance for the overall OER process.^[39,40] The adsorption resistance is dependent on the applied potential and catalyst and may be negligible in some cases. In such cases, the EEC can be simplified to the Randle's model. The characteristic frequency of the active site for OER in the R-Mix and R-LCTCo0.11 samples is determined to be 60 Hz at 1.7 V versus RHE, as shown in Figure 6A. On the other hand, the characteristic frequency for OER in the remaining three samples is much lower, ranging from 3 to 6 Hz at the same potential, indicating a slower reaction rate. The corresponding Nyquist plots in Figure 6B demonstrate that R-Mix and R-LCTCo0.11 have lower R_{ct} values compared to the other three samples. To clarify, the fitting parameters of R_{ct} for these samples are shown in Figure 6C and ranked as follows: R-LCTCo0.11 (58 Ω) < R-Mix (82 Ω) < LCTCo0.11 (931 Ω) < Mix (1023 Ω) < LCT (1485 Ω). The lower R_{ct} value indicates higher catalytic and kinetic activity for OER, which is total in concordance to the LSV and Tafel data displayed in Figure 3.

3. Conclusion

In summary, a series of Co-doped titanate perovskite with A-site deficiency is successfully synthesized by a sol-gel method, and Co nanoparticle-anchored perovskites are obtained via further calcination in a tubular furnace under a 5% H_2/N_2 atmosphere. The size and population density of exsolved Co nanoparticles are discovered to be highly dependent on Co doping level (crystal structure), reduction temperature and time. The catalyst (R-LCTCo0.11) reduced at 800 °C for 2 h with proper Co nanoparticle size and density exhibits superior OER catalytic performance. Notably, the mass activity of R-LCTCo0.11 (1700 $mA\ mg^{-1}$ at $\eta = 450\ mV$) is 17-times and 3-times higher than that of LCTCo0.11 (97 $mA\ mg^{-1}$) and R-Mix (560 $mA\ mg^{-1}$), respectively. This suggests that the exsolution method outperforms the physical mixture of samples, and the exsolved Co nanoparticles significantly promote OER performance. Then, LCTCo0.11 exhibits excellent stability with 10 h chronopotentiometry test at $j = 10\ mA\ cm^{-2}$ and 1000 cycles of CV. Furthermore, the smaller

charge transfer resistance ($R_{ct} = 58\ \Omega$) of R-LCTCo0.11 implies the higher catalytic and kinetic activity for OER. This novel catalyst could provide a promising strategy for improving the atom utilization efficiency in OER and other systems such as HER and ORR.

4. Experimental Section

Materials Synthesis and Characterization: Samples of LCTCo $_x$, $x = 0.01, 0.05, 0.11, 0.2,$ and 0.3 were prepared by a modified sol-gel method.^[41–43] First, appropriate amount of Titanium (IV) bis(ammonium lactato) dihydroxide solution (Sigma-Aldrich, 50 wt. % in H_2O) and ethylene glycol (Fisher Chemical, LR) were measured and mixed under magnetic stirring. Second, desired amounts of citric acid (Acros Organics, 99.5%) were added to the solution as a chelating agent following 5 mL distilled water to accelerate its dissolution. Third, stoichiometric amounts of $La(NO_3)_3 \cdot 6H_2O$ (Alfa-Aesar, 99.9%), $Ca(NO_3)_2 \cdot 4H_2O$ (Alfa-Aesar, 99%), $Co(NO_3)_2 \cdot 6H_2O$ (Acros Organics, 99%) were dissolved in deionized water and added into the above solution under continuous heating and stirring. The molar ratio of total metal ions/citric acid/ethylene glycol was 1:2:12. The resulting solution was kept on a hot plate at $\approx 120\ ^\circ C$ with continuous magnetic stirring to form a viscous gel and then the gel was heated at 300 °C overnight. During this process, most of the organics in the solution would have been carbonized. The residue was calcined at 550 °C for 2 h for decarbonization. Finally, the LCTCo $_x$ samples were obtained by calcinating the precursors at 1000 °C for 8 h in a Muffle furnace. The cobalt-exsolved LCTCo $_x$ (R-LCTCo $_x$) samples were produced by reducing them in a tubular furnace under a 5% H_2/N_2 atmosphere. Particularly, to optimize the OER performance of the catalyst, a series of doping levels, reduction times and temperatures had also been investigated. Meanwhile, control samples $La_{0.2}Ca_{0.7}TiO_3$ (LCT) and CoO $_y$ were synthesized by the same method shown above. The Mix sample was produced by mixing appropriate amount of LCT and CoO $_y$ with the Ti:Co ratio of 0.89:0.11. To get R-Mix sample, the Mix sample was reduced in a tubular furnace at 800 °C for 2 h with the atmosphere of 5% H_2/N_2 .

The crystal structures of all the as-prepared samples were examined using a PANalytical Empyrean X-ray diffractometer with $Cu-K\alpha 1$ radiation and zero-background Si substrate holder. The Brunauer-Emmett-Teller (BET) specific surface area was determined by measurements of N_2 adsorption/desorption on a Micromeritics TriStar II 3020 at 77K and the pore size distributions were analyzed by the Barrett-Joyner-Halenda (BJH) method. The morphological structures of catalysts were characterized by a scanning electron microscope (SEM, Jeol JSM-IT800) equipped with X-ray energy dispersive spectrometers (EDS) and a Aberration-corrected Scanning Transmission Electron Microscopy (STEM, FEI Titan Themis TEM) also equipped with EDS. Thermogravimetric analysis (TGA) of catalysts was performed using Netzsch STA 449C in air with the flowrate of 30 $ml\ min^{-1}$ to 700 °C with the heating rate of 5 °C min^{-1} .

Electrochemical Measurements: All electrochemical measurements were conducted on a typical three-electrode system using an electrochemical workstation (AMETEK). A Pt plate and an Ag/AgCl (filled with saturated KCl) electrode were used as the counter and reference electrodes, respectively. A glassy carbon electrode (GCE, inner diameter 3 mm, outer diameter 5 mm) loaded with catalyst ink was served as the working electrode. The catalyst ink was made by mixing 4 mg catalyst, 8 mg carbon black, 60 μL 5 wt.% Nafion solution (Sigma-Aldrich) and 940 μL anhydrous ethanol processing for at least 30 min sonication. The catalyst ink was dropped casted onto the polished GCE and dried in air at room temperature. Linear sweep voltammetry (LSV) curves were recorded in 1.0 M KOH electrolyte from 1.2 to 1.9 V versus Reversible Hydrogen Electrode (RHE) with iR -correction at a scan rate of 10 $mV\ s^{-1}$. Electrochemically active surface area (ECSA) was estimated by scanning CV from 1.22 to 1.32 V versus RHE (non-Faradaic region) at different scan rates ranging from 10 to 200 $mV\ s^{-1}$. Electrochemical impedance spectroscopy (EIS) was collected from 100000 to 0.1 Hz at a series of voltages. The electrochemical

stability was characterized by chronopotentiometry at a current density of 10 mA cm⁻² and 1000 cycles of CV between 1.3 and 1.9 V versus RHE.

Supporting Information

Supporting Information is available from the Wiley Online Library or from the author.

Acknowledgements

The authors acknowledge the support from Fundamental Research Funds for Engineering and Physical Sciences Research Council (EPSRC) Critical Mass grant EP/R023522/1, Light element Analysis Facility Grant EP/T019298/1, Strategic Equipment Resource grant EP/R023751/1, and China Scholarship Council (CSC).

Conflict of Interest

The authors declare no conflict of interest.

Data Availability Statement

We will set up and share doi on our Pure system to make data openly available before the manuscript would be published

Keywords

exsolution, mass activities, oxygen evolution reaction, perovskites, water electrolysis

Received: October 9, 2023

Published online:

- [1] C. Si, W. Zhang, Q. Lu, E. Guo, Z. Yang, J. Chen, X. He, J. Luo, *Catalysts* **2022**, 12, 601.
- [2] G. Chen, Y. Zhu, H. M. Chen, Z. Hu, S. F. Hung, N. Ma, J. Dai, H. J. Lin, C. T. Chen, W. Zhou, *Adv. Mater.* **2019**, 31, 1900883.
- [3] J. Song, C. Wei, Z.-F. Huang, C. Liu, L. Zeng, X. Wang, Z. J. Xu, *Chem. Soc. Rev.* **2020**, 49, 2196.
- [4] N.-T. Suen, S.-F. Hung, Q. Quan, N. Zhang, Y.-J. Xu, H. M. Chen, *Chem. Soc. Rev.* **2017**, 46, 337.
- [5] Y. Li, G. Chen, Y. Zhu, Z. Hu, T. S. Chan, S. She, J. Dai, W. Zhou, Z. Shao, *Adv. Funct. Mater.* **2021**, 31, 2103569.
- [6] L. Fei, H. Sun, X. Xu, Y. Li, R. Ran, W. Zhou, Z. Shao, *Chem. Eng. J.* **2023**, 471, 144660.
- [7] S. She, Y. Zhu, X. Wu, Z. Hu, A. Shelke, W.-F. Pong, Y. Chen, Y. Song, M. Liang, C.-T. Chen, H. Wang, W. Zhou, Z. Shao, *Adv. Funct. Mater.* **2022**, 32, 2111091.
- [8] J. Hwang, R. R. Rao, L. Giordano, Y. Katayama, Y. Yu, Y. Shao-Horn, *Science* **2017**, 358, 751.
- [9] B. Zhang, X. Zheng, O. Voznyy, R. Comin, M. Bajdich, M. García-Melchor, L. Han, J. Xu, M. Liu, L. Zheng, F. P. García De Arquer, C. T. Dinh, F. Fan, M. Yuan, E. Yassitepe, N. Chen, T. Regier, P. Liu, Y. Li, P. De Luna, A. Janmohamed, H. L. Xin, H. Yang, A. Vojvodic, E. H. Sargent, *Science* **2016**, 352, 333.
- [10] G. Zhang, G. Liu, L. Wang, J. T. S. Irvine, *Chem. Soc. Rev.* **2016**, 45, 5951.
- [11] J. Suntivich, K. J. May, H. A. Gasteiger, J. B. Goodenough, Y. Shao-Horn, *Science* **2011**, 334, 1383.
- [12] Y. Wang, X. Shen, H. Arandiyani, Y. Yin, F. Sun, X. Chen, M. Garbrecht, L. Han, G. G. Andersson, C. Zhao, *J. Power Sources* **2020**, 478, 228748.
- [13] X. Li, H. Wang, Z. Cui, Y. Li, S. Xin, J. Zhou, Y. Long, C. Jin, J. B. Goodenough, *Sci. Adv.* **2019**, 5, 6262.
- [14] J. G. Lee, J. Hwang, H. J. Hwang, O. S. Jeon, J. Jang, O. Kwon, Y. Lee, B. Han, Y.-G. Shul, *J. Am. Chem. Soc.* **2016**, 138, 3541.
- [15] E. Da Rosa Silva, M. Curi, J. V. Nicolini, J. G. Furtado, A. R. Secchi, H. C. Ferraz, *Ceram. Int.* **2021**, 47, 13331.
- [16] J.-I. Jung, M. Risch, S. Park, M. G. Kim, G. Nam, H.-Y. Jeong, Y. Shao Horn, J. Cho, *Energy Environ. Sci.* **2016**, 9, 176.
- [17] H. Zhang, D. Guan, X. Gao, J. Yu, G. Chen, W. Zhou, Z. Shao, *J. Mater. Chem. A* **2019**, 7, 19228.
- [18] L. Xu, Q. Jiang, Z. Xiao, X. Li, J. Huo, S. Wang, L. Dai, *Angew. Chem., Int. Ed.* **2016**, 128, 5363.
- [19] Y. Li, G. Chen, H.-C. Chen, Y. Zhu, L. Fei, L. Xu, T. Liu, J. Dai, H. Huang, W. Zhou, Z. Shao, *Energy Environ. Sci.* **2023**, 16, 3331.
- [20] Y.-F. Sun, J.-H. Li, L. Cui, B. Hua, S.-H. Cui, J. Li, J.-L. Luo, *Nanoscale* **2015**, 7, 11173.
- [21] S. Liu, Q. Liu, J.-L. Luo, *ACS Catal.* **2016**, 6, 6219.
- [22] Y. Li, B. Hu, C. Xia, W. Q. Xu, J. P. Lemmon, F. Chen, *J. Mater. Chem. A* **2017**, 5, 20833.
- [23] K.-Y. Lai, A. Manthiram, *Chem. Mater.* **2018**, 30, 2515.
- [24] C. Xu, W. Sun, R. Ren, X. Yang, M. Ma, J. Qiao, Z. Wang, S. Zhen, K. Sun, *Appl. Catal., B* **2021**, 282, 119553.
- [25] Y. Gao, D. Chen, M. Saccoccio, Z. Lu, F. Ciucci, *Nano Energy* **2016**, 27, 499.
- [26] Y. Zhu, W. Zhou, R. Ran, Y. Chen, Z. Shao, M. Liu, *Nano Lett.* **2016**, 16, 512.
- [27] Y. Zhu, T. Liu, Y. Wang, X. Zhang, C. Ren, W. Li, S. Wang, *Sustainable Energy Fuels* **2022**, 6, 1373.
- [28] S. Park, Y. Kim, Y. Noh, T. Kim, H. Han, W. Yoon, J. Choi, S.-H. Yi, W.-J. Lee, W. B. Kim, *J. Mater. Chem. A* **2020**, 8, 138.
- [29] D. Neagu, G. Tsekouras, D. N. Miller, H. Ménard, J. T. S. Irvine, *Nat. Chem.* **2013**, 5, 916.
- [30] G. Tsekouras, D. Neagu, J. T. S. Irvine, *Energy Environ. Sci.* **2013**, 6, 256.
- [31] K. S. W. Sing, *Pure Appl. Chem.* **1985**, 57, 603.
- [32] H. Zhu, J. Luo, J. Liang, G. Rao, J. Li, J. Zhang, Z. Du, *Phys. B* **2008**, 403, 3141.
- [33] G. Li, S. Hou, L. Gui, F. Feng, D. Zhang, B. He, L. Zhao, *Appl. Catal., B* **2019**, 257, 117919.
- [34] H.-Y. Wang, S.-F. Hung, H.-Y. Chen, T.-S. Chan, H. M. Chen, B. Liu, *J. Am. Chem. Soc.* **2016**, 138, 36.
- [35] J. G. Lee, J.-H. Myung, A. B. Naden, O. S. Jeon, Y. G. Shul, J. T. S. Irvine, *Adv. Energy Mater.* **2020**, 10, 1903693.
- [36] J. Wang, Y. Gao, D. Chen, J. Liu, Z. Zhang, Z. Shao, F. Ciucci, *ACS Catal.* **2018**, 8, 364.
- [37] J. Zhang, X. Li, Y. Liu, Z. Zeng, X. Cheng, Y. Wang, W. Tu, M. Pan, *Nanoscale* **2018**, 10, 11997.
- [38] S. Watzela, A. S. Bandarenka, *Electroanalysis* **2016**, 28, 2394.
- [39] S. Anantharaj, S. Noda, *ChemElectroChem* **2020**, 7, 2297.
- [40] V. Maruthapandian, S. Kumaraguru, S. Mohan, V. Saraswathy, S. Muralidharan, *ChemElectroChem* **2018**, 5, 2795.
- [41] B.-G. Park, *Chem. Phys. Lett.* **2019**, 722, 44.
- [42] Z. Du, P. Yang, L. Wang, Y. Lu, J. B. Goodenough, J. Zhang, D. Zhang, *J. Power Sources* **2014**, 265, 91.
- [43] P. Vaqueiro, M. A. López-Quintela, *Chem. Mater.* **1997**, 9, 2836.